SideSense: Robust Physiological Motion Detection via mmWave Joint Communication and Sensing Systems With Multiple Beams

Mohammad Shadman Ishrak, *Graduate Student Member, IEEE*, Jannatun Noor Sameera, *Graduate Student Member, IEEE*, Alvin Yang, *Graduate Student Member, IEEE*, Yanjun Pan, *Member, IEEE*, Yao Zheng, *Member, IEEE*, Olga Borić-Lubecke, *Fellow, IEEE*, and Victor M. Lubecke, *Fellow, IEEE*

***Abstract*—A 28-GHz multibeam joint communication and sensing system called SideSense is presented, in which a line-of-sight (LoS) beam is used to maintain reliable communication, while other sensing beams are used to enhance physiological motion detection. SideSense decodes the motion frequency and shape from the channel state information (CSI) by first tuning the gain ratio and phase differences between the LoS communication beam and non-LoS (NLoS) beam to maximize the sensing signal-to-noise ratio (SSNR) without significantly degrading the communication channel capacity (CCC). Analytical results based on a bistatic model are presented to show a gain ratio of around 1 and a phase difference of 90° or 270°, which are ideal for optimizing both SSNR and CCC. Experiments based on an array of phased array (APA) beamformers and orthogonal frequency-division multiplexing (OFDM) waveforms with phantom and human subjects are presented to validate the performance of SideSense. Results show that SideSense can improve SSNR by 84% while reducing CCC by 35%, an acceptable decrease within the normal operational parameters of a millimeter-wave (mmWave) communication system, which would not trigger a link reestablishment procedure, e.g., communication beam realignment.**

***Index Terms*—Biosensors, channel state information (CSI) amplitude, future generation (FutureG) wireless, millimeter wave (mmWave), multiple beam, vital signs sensing.**

I. Introduction

THE concept of radio systems that support both radar sensing and communication functions by sharing spectrum and hardware has been known for decades [1]. More recent studies have demonstrated that existing IEEE 802.11ay access points can be retrofitted to perform high-accuracy human detection and sensing [2]. This principle of joint communications and sensing (JCS) has been demonstrated for accurate target location and tracking while maintaining high communication throughput at microwave frequencies [3], [4]. Millimeter-wave (mmWave) JCS has attracted significant attention for future generation (FutureG) cellular networks due to the benefits of reduced cost, size, weight, and improved spectral efficiency [5], [6], while achieving both communication and radar sensing capabilities through shared hardware and signal processing modules [7], [8]. The ability to obtain accurate positions, speeds, and other features for objects while simultaneously maintaining reliable communication links is of immense importance for emerging applications, such as continuous health monitoring, smart cars, remote aerial vehicles, and augmented reality [6], [9], [10].

There has been demonstrated success in the design of mmWave systems for unobtrusive continuous physiological monitoring, including applications in assistive devices, in-cabin vehicle occupant monitoring, sleep studies, vital signs monitoring, and stress level monitoring [11], [12], [13], [14], [15], [16], [17], [18]. The potential compactness of hardware at higher frequencies enables practical implementation of antenna arrays, which can be used for digital beamforming and multiple-input multiple-output (MIMO) system configurations for signal separation from multiple individuals [19], [20], [21], [22]. Moreover, the large bandwidth potentially provides high data rate communications for real-time delivery and feedback of the biomedical data acquired by the sensing modality. Recent experimental work has shown that 5G signals can be leveraged for joint radar and communication functions [23].

The primary design challenge in mmWave JCS systems lies in the diversity of beam management requirements for communications and sensing [24], [25]. Line-of-sight occlusion and clock asynchrony are notable obstacles to both communication and sensing [26]. The mmWave communication protocol consists of an initial beam alignment process for both the transmitter (TX) and receiver (RX) to identify the optimal beamforming angles that maximize the link budget, and beam realignment is performed only if the link budget deteriorates

Received 26 June 2025; accepted 8 July 2025. This work was supported in part by the National Science Foundation (NSF) under Grant CNS-2039089, Grant IIS-1915738, and Grant OAC-2417891; and in part by the Naval Information Warfare Center Pacific (NIWC) Pacific and TMY Technology Inc. *(Corresponding author: Mohammad Shadman Ishrak.)*

This work involved human subjects or animals in its research. Approval of all ethical and experimental procedures and protocols was granted by the University of Hawaii CHS under Protocol No. 14884.

Mohammad Shadman Ishrak, Jannatun Noor Sameera, Alvin Yang, Yao Zheng, Olga Borić-Lubecke, and Victor M. Lubecke, are with the Department of Electrical and Computer Engineering, University of Hawai'i at Manoā, Honolulu, HI 96822 USA (e-mail: ishrak@hawaii.edu; jsameera@hawaii.edu; ayang27@hawaii.edu; yaozheng@hawaii.edu; lubecke@hawaii.edu; olgabl@hawaii.edu).

Yanjun Pan is with the Department of Electrical Engineering and Computer Science, University of Arkansas Fayetteville, Fayetteville, AR 72701 USA (e-mail: yanjunp@uark.edu).

Digital Object Identifier 10.1109/TMTT.2025.3589906

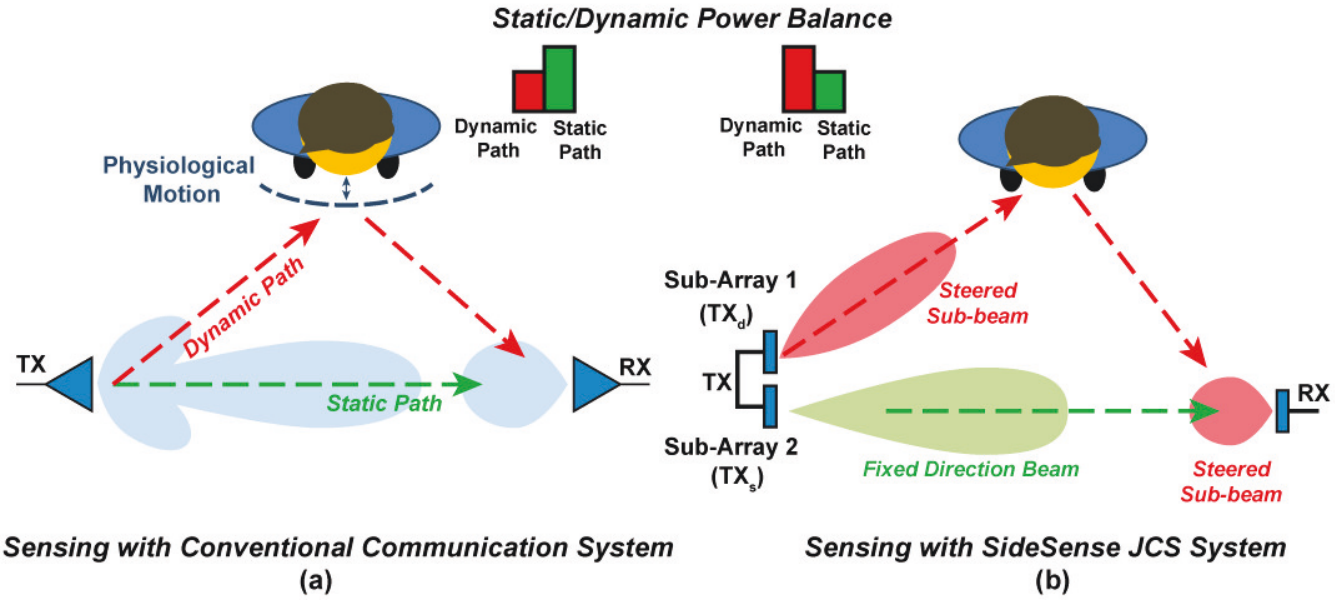

Fig. 1. Comparison of sensing in conventional communication systems versus the SideSense JCS system. (a) Illustrates a conventional system where the dynamic path produced by the sidelobe senses the physiological motion, resulting in a less efficient power balance between the static communication path and the dynamic path. (b) Shows the SideSense JCS system with an array of beam steering subarrays (TX$_s$ and TX$_d$), where the system leverages both steered subbeams of the TX to produce balanced static and dynamic paths, achieving better power distribution between the communication and sensing accuracy.

significantly [27], [28]. On the other hand, sensing requires time-varying continuous beam scanning and tracking to follow an object. Prior research mostly considers schemes that use a single-phased array for both communications and sensing [29], [30], [see Fig. 1(a)] which either limits the sensing direction or utilizes expensive full digital arrays to synthesize complicated beam patterns to meet the requirements of JCS [31].

Instead, this work explores a cost-efficient analog multibeam technology, e.g., an array of phased arrays (APAs), [32], [33], [34], [35], to enable low-cost and efficient implementation of JCS for physiological motion sensing. The JCS APA system proposed here consists of multiple analog subarrays connected to a single RF chain, allowing the signal to be transmitted via a beam pattern with multiple arms. One subbeam, fixed in direction, supports communications, while the other subbeam supports direction-varying scans to locate and sense the target, as illustrated in Fig. 1(b).

While the hardware architecture is straightforward, power allocation and phase coordination among subbeams are challenging, as they are critical for the recovery of physiological motion from the channel measurements obtained by the JCS system. Hence, presented here is a comprehensive framework, SideSense, based on the original theoretical results of a bistatic multipath JCS channel, to optimize both physiological motion detection sensitivity and communication link capacity. The optimal power to gain ratio between the communication and sensing subbeams [see Fig. 1(b)] is identified, as well as their phase difference, and a three-step tuning protocol is provided in SideSense to jointly optimize communication and sensing performance.

SideSense is implemented here using 28-GHz beamformers and software-defined radios (SDRs). With experiments performed using phantom devices and human subjects, SideSense is shown to improve the sensing signal-to-noise ratio (SSNR) by 84% compared to a single-beam JCS counterpart while only reducing the communication channel capacity (CCC) by 35%, which is an acceptable decrease that would not trigger a link reestablishment procedure [36], [37], [38]. The rest of this article is organized as follows. Section II provides necessary background information on channel measurement in mmWave communication systems and on the JCS system model. Section III introduces SideSense, including bistatic JCS channel analysis insights and protocol design. Section IV presents the SideSense prototype and experimental results. Section V concludes the findings.

II. Physiological Sensing via CSI

Implementation of JCS can be designed to leverage the channel measurement process that is part of nearly all communication protocols. For instance, in mmWave cellular networks, a cellular base station (gNB) uses phased arrays with multiple antenna elements to create highly directional signal beams toward users, allowing concurrent communication through spatial multiplexing to user equipment (UE). To improve reliability, the gNB broadcasts reference signals for the UE to measure and feedback channel state information (CSI), which the gNB uses to adjust the signal beams and track users. As users frequently move, channel measurements are performed more regularly in mmWave cellular systems than in sub-6 GHz counterparts to assist beam alignment and beam tracking.

A. MmWave Channel State Information

The CSI represents the channel properties of a radio link, which describes how a signal propagates from a TX to an RX, including the combined effects of scattering, fading, and power decay with distance. In 5G new radio (NR), CSI is obtained through the CSI reference signal (CSI-RS), which is embedded

in packets broadcast via the physical data shared channel (PDSCH). For each subcarrier k in an orthogonal frequency-division multiplexing (OFDM) system, the RX compares the received signal with the reference signal to compute the CSI and can be represented as

$$h_k = |h_k| \, e^{j \angle h_k} \tag{1}$$

where $|h_k|$ and $\angle h_k$ are the amplitude and phase of the channel responses at subcarrier k, respectively. Table I shows the list of symbols used in equations and their meanings in this work.

B. Extracting Physiological Motion From CSI

Since the CSI represents how the surroundings affect the signal, it is possible to detect physiological motion, such as that from breathing and heartbeat, via changes in amplitude and phase. However, real-world mmWave CSI is often the composite effect of multiple propagation paths, which complicates the physiological motion detection process. Specifically, CSI captures the combined effect of all the paths a radio wave takes as it travels, which can be broken down into static and dynamic components. The static component includes the line-of-sight (LoS) path and reflections from stationary objects in the environment, while the dynamic component represents reflections from a moving subject, such as the torso of a human when breathing.

The mathematical model of CSI amplitude and phase at subcarrier k in the presence of multipath is represented as [29]

$$\begin{aligned} |h_k(t)| &= \left| h_{k,s} + h_{k,d} \right| \\ &= \sqrt{\left|h_{k,s}\right|^2 + \left|h_{k,d}(t)\right|^2 + 2\left|h_{k,s}\right|\left|h_{k,d}(t)\right| \cos\left(\Delta\varphi(t)\right)} \end{aligned} \tag{2}$$

where $h_{k,s}$ and $h_{k,d}$ are the static and dynamic components, respectively, of the CSI at the subcarrier k. The function $\Delta\varphi(t)$ is the phase difference between the static and dynamic components, and can be represented by

$$\Delta\varphi(t) = \frac{2\pi\left(d_d(t) - d_s\right)}{\lambda_k} \tag{3}$$

where d_s denotes the length of the static path, $d_d(t)$ represents the length of the time-varying dynamic path generated by the moving object, and λ_k represents the wavelength of the subcarrier k.

Thus, the CSI amplitude is modulated, and the range of its change due to the moving object mainly depends on the relative strength between the static and dynamic paths. The CSI phase also exhibits a similar modulation effect due to the moving object. It is worth noting that the detection performance of CSI phase and amplitude waveforms is complementary to each other, with some offset depending on the object's location. Specifically, for locations where the CSI amplitude exhibits a limited dynamic range for sensing, the CSI phase provides a favorable dynamic range for satisfactory detection performance.

III. SideSense: Theory and Design

This section provides the analysis and design of a multibeam JCS system, SideSense, which leverages the hardware capability of an APA to perform better physiological motion detection compared to single-beam systems, without compromising the link reliability for communication. The APA architecture used by SideSense is compatible with emerging standards, such as 5G NR and 802.11af/h, which employ multibeam hardware to enhance mmWave signal coverage [39], [40].

A. SideSense Design: Engineering CSI for JCS

Consider a TX equipped with two uniform linear arrays (ULAs) that are connected with a single RF chain, as shown in Fig. 1, where there are N antenna elements for each ULA. For simplicity, assume that the ULA at TX_d, which points to the target, creates the dynamic component for the composite CSI at the RX, while the ULA at TX_s, which establishes the LoS link with the RX, creates the static component. Subcarrier subscript k and time variable t are dropped in the dynamic component for simplicity. The received signal at the omnidirectional RX can be represented as

$$y = \mathbf{h}_s^T \mathbf{w_s} x + \mathbf{h}_d^T \mathbf{w_d} x + z \tag{4}$$

where $\mathbf{h}_s$, $\mathbf{w}_s$, $\mathbf{h}_d$, and $\mathbf{w}_d$ are all N-by-1 vectors, representing the channel from the N transmit antennas and the beamforming weights for the ULA that create the static and dynamic components, respectively. The symbol x is the transmitted signal, and z represents the channel noise.

For a typical ULA, the space between the antenna elements, d, is half the wavelength, which is significantly shorter than the link distance, especially in mmWave bands. Hence, the communication is in the far-field, where the channel can be decomposed into a gain component that is consistent across all the antenna elements in the ULA, and a phase component. With the decomposed channel, (4) can be rewritten as

$$\mathbf{y} = a_s \left[e^{j\frac{2\pi n d}{\lambda}\sin(\phi_s)} \right]^N \mathbf{w}_s x + a_d \left[e^{j\frac{2\pi n d}{\lambda}\sin(\phi_d)} \right]^N \mathbf{w}_d x + z \tag{5}$$

where a_s and a_d are the channel gains for the static and dynamic channel components, respectively. Also, $[\cdot]^N$ represents a row vector of size N, and $[e^{j(2\pi n d/\lambda)\sin(\phi_s)}]^N$ and $[e^{j(2\pi n d/\lambda)\sin(\phi_d)}]^N$ are the channel phases for the static and dynamic channel components, respectively, for $n = 0, 1, \ldots, N-1$, with the corresponding angle-of-departure (AoD) denoted as ϕ_s and ϕ_d. Specifically, the phase component $[e^{j(2\pi n d/\lambda)\sin(\phi_s)}]^N$ or $[e^{j(2\pi n d/\lambda)\sin(\phi_d)}]^N$ is the steering vector for the ULA beamforming. The beamforming weights for the ULA are complex values, which can be denoted as

$$\mathbf{w}_s = \left[g_{s,0} e^{j\theta_{s,0}}, g_{s,1} e^{j\theta_{s,1}}, \ldots, g_{s,N-1} e^{j\theta_{s,N-1}} \right]^T \tag{6}$$

$$\mathbf{w}_d = \left[g_{d,0} e^{j\theta_{d,0}}, g_{d,1} e^{j\theta_{d,1}}, \ldots, g_{d,N-1} e^{j\theta_{d,N-1}} \right]^T \tag{7}$$

where $|g_{s,n}| \leq 1$ and $|g_{d,n}| \leq 1$ for $n = 0, 1, \ldots, N-1$.

To maximize the directionality gain toward the AoD ϕ, the complex conjugation of the steering vector at ϕ should be used as the codebook entry to form a beam, that is,

$$\mathbf{w}_{\phi_s}^T = \left[e^{-j\frac{2\pi n d}{\lambda}\sin(\phi_s)} \right]^N \tag{8}$$

Algorithm 1 Sensing SNR

1: **procedure** SSNR($\mathbf{h}^M$, f_{phy})
2: $H(f) \leftarrow \text{FFT}(\mathbf{h}^M)$
3: $\text{SSNR} \leftarrow \frac{H(f=f_{\text{phy}})}{\text{E}(H(f\neq f_{\text{phy}}))}$
4: **return** SSNR
5: **end procedure**

$$\mathbf{w}_{\phi_d}^T = \left[e^{-j\frac{2\pi nd}{\lambda}\sin(\phi_d)}\right]^N \tag{9}$$

where the index of the subcarrier k is omitted for simplicity.

In particular, the global phase offsets Δ_s and Δ_d for the static and dynamic components, respectively, tune the arriving phase of each channel component at the RX. Introducing the global phase offset into the optimal beamforming weights in (8) and (9) results in the beamforming weights represented in the following equations, which do not change the steering directions ϕ_s and ϕ_d but introduce an additional phase offset Δ_s and Δ_d for the static and dynamic components at the RX:

$$\mathbf{w}'_{\phi_s} = \mathbf{w}_{\phi_s} e^{\Delta_s} \tag{10}$$

$$\mathbf{w}'_{\phi_d} = \mathbf{w}_{\phi_d} e^{\Delta_d}. \tag{11}$$

Similarly, the global phase offset can be introduced into the generalized beamforming weights expressed in (6) and (7).

By combining (5)–(7) and global phase offsets, the ratio of static and dynamic components of the composite CSI, which consists of the effects of APA and the wireless channel, can be represented as

$$\frac{|h_s|}{|h_d|} = \frac{\left|a_s \sum_{n=0}^{N-1} g_{s,n} e^{j\left(\frac{2\pi nd}{\lambda}\sin(\phi_s)+\theta_s,n+\Delta_s\right)}\right|}{\left|a_d \sum_{n=0}^{N-1} g_{d,n} e^{j\left(\frac{2\pi nd}{\lambda}\sin(\phi_d)+\theta_d,n+\Delta_d\right)}\right|}. \tag{12}$$

From (12), it is observed that with the beamforming weights and global phase offsets, the detection performance of sensing activities with CSI can be tuned on two levels, which is the theoretical guideline behind the design of SideSense. First, the beamforming weights can be adjusted to modify the gain ratio between the static and dynamic components. Moreover, the global phase offsets can also be utilized to tune the phase difference between the static and dynamic components.

SideSense consists of three subprocedures (see Fig. 2), unimodal beam sweep, unimodal gain ratio tuning, and unimodal global phase offset tuning, which perform time-varying continuous beam scanning for sensing once the LoS subbeam is aligned with the RX via the standard beam alignment process. Let $\mathbf{h}^M = h(1), h(2), \ldots, h(M)$ represent M samples of the composite CSI that include both static and dynamic components, and let H be the frequency-domain fast Fourier transform (FFT) of $\mathbf{h}^M$. A function is first defined to compute the SSNR for physiological motion detection in Algorithm 1, where f_{phy} is the frequency of the physiological motion and $E(\cdot)$ is the expectation.

The procedure begins after the communication protocol finishes the standard beam alignment process. The first part utilizes the sensing subbeam and carries out a sweep to identify the target using the unimodal beam sweep process detailed from Lines 2 to 17 in Algorithm 2, where Ψ_b is a termination threshold for the beam sweep. Next, SideSense adjusts the array gain while monitoring the CSI on the in-phase and

Algorithm 2 SideSense

1: /* *Unimodal Beam Sweep* */
2: **for** $t = 1, 2, \ldots,$ **do**
3: Select the beam direction with index $k(t)$
4: Obtain DELzz- DELM samples of the composite CSI by applying the steering vector of $k(t)$: $\mathbf{h}^M(t) \leftarrow \mathbf{h}^M(\mathbf{w}_{k(t)})$
5: Evalu- ate the SSNR

$$\text{SSNR}(t) \leftarrow \text{SSNR}\left(\mathbf{h}^M(t), f_{\text{phy}}\right)$$

6: **if** $t == 1$ **then**
7: $\text{SSNR}_{\max} \leftarrow \text{SSNR}(t)$
8: $\psi_b(t) \leftarrow \text{SSNR}(t)$
9: **else**
10: $\text{SSNR}_{\max} \leftarrow \max(\{\text{SSNR}(1), \ldots, \text{SSNR}(t-1)\})$
11: $\psi_b(t) \leftarrow \text{SSNR}(t) - \text{SSNR}_{\max}$
12: **end if**
13: **if** $\psi_b(t) \leq \Psi_b$ **then**
14: $k^* \leftarrow k(t)$
15: Terminate the beam sweep
16: **end if**
17: **end for**
18: /* *Unimodal Gain Ratio Tuning* */
19: **for** $t = 1, 2, \ldots,$ **do**
20: **if** $t == 1$ **then**
21: Get the steer- ing vector for beam index k^*

$$\mathbf{w}(t) \leftarrow \mathbf{w}_{k^*}$$

22: **else**
23: Update the steering vector

$$\mathbf{w}(t) \leftarrow (1 + \delta g)\mathbf{w}(t-1)$$

24: Evaluate $\psi_g(t) \leftarrow \left|\frac{|h_s(\mathbf{w}(\mathbf{t}))|}{|h_d(\mathbf{w}(\mathbf{t}))|} - 1\right|$
25: **end if**
26: **if** $\psi_g(t) \leq \Psi_g$ **then**
27: $\mathbf{w}^* \leftarrow \mathbf{w}(t)$
28: Terminate the gain tuning
29: **end if**
30: **end for**
31: /* *Unimodal Global Phase Offset Tuning* */
32: **for** $t = 1, 2, \ldots,$ **do**
33: **if** $t == 1$ **then**
34: $\mathbf{w}(t) \leftarrow \mathbf{w}^*$
35: **else**
36: Update the steering vector: $\mathbf{w}(t) \leftarrow e^{\delta\phi}\mathbf{w}(t-1)$
37: Evaluate $\psi_p(t) \leftarrow |\angle\frac{\mathbf{h}_s(\mathbf{w}(t))}{\mathbf{h}_d(\mathbf{w}(t))} - 90|$
38: **end if**
39: **if** $\psi_p(t) \leq \Psi_p$ **then**
40: $\mathbf{w}^* \leftarrow \mathbf{w}(t)$
41: Terminate the phase tuning
42: Proceed to physiological motion sensing with the steering vector $\mathbf{w}^*$
43: **end if**
44: **end for**

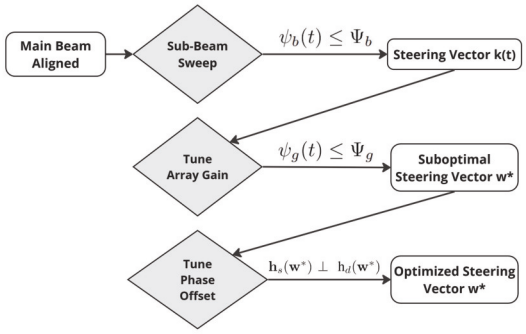

Fig. 2. SideSense flowchart with three subprocedures.

quadrature (IQ) plot until the origin shifts outside the CSI circle, following the procedures from Lines 19 to 30. δg is an incrementing step and Ψ_g is a termination threshold. After the gain tuning, SideSense obtains the suboptimal steering vector $\mathbf{w}^*$ as the warm start for the following phase tuning process. Finally, the SideSense system further updates the steering vector $\mathbf{w}^*$ with the tuned array gain by adjusting the global phase offset until the corresponding static channel vector, $\mathbf{h}_s(\mathbf{w}^*)$, and the dynamic channel arc, $\mathbf{h}_d(\mathbf{w}^*)$, are orthogonal. Define an incrementing step $\delta\phi$ and a termination threshold Ψ_p for the final phase tuning process, which is detailed from Lines 32 to 44. After the three-part procedure, physiological motion is sensed by collecting the CSI using the optimized steering vector, $\mathbf{w}^*$, with tuned array gain and phase. The amplitude of the collected CSI is then processed to recover the physiological motion frequency and waveform.

B. Simulation Study: Benefits of Multibeam

To ease the analysis, SideSense was modeled as a bistatic JCS system model, with two antennas, TX_s and TX_d, connecting to the same RF chain and one RX [see Fig. 1(b)]. As mmWave frequencies have high path loss, the TX, modeling a gNB, uses phased arrays to generate a highly directional beam to account for the loss. For SideSense, the TX employs a low-cost APA architecture to generate multiarm beam patterns. The RX, modeling a cellular UE or Wi-Fi client, uses a small phased array to create a semi-directional beam to improve reception due to the device size limitation.

The system model allows separate control of the communication and sensing subbeams at TX based on the in situ requirements and dynamically adjusts the gains and phases of the subbeams to optimize the communication and sensing results. Specifically, SideSense TX can adjust the subbeams' gain ratio phases to improve the dynamic range of the CSI amplitude. It can also adjust the subbeams' initial phase to mitigate the null position issue of a bistatic JCS. Both benefits are studied with simulations and elaborated below.

1) Gain Ratio Tuning: Consider the two cases shown in Fig. 3(a) and (b). For case a, the ratio, $|h_{k,s}|/|h_{k,d}|$, is small, and the CSI arc contains the coordinate origin, and the overall CSI amplitude does not change significantly as the dynamic component of the CSI rotates due to physiological motion. For case b, the ratio, $|h_{k,s}|/|h_{k,d}|$, is large. The origin of the static vector is outside of the CSI circle, and the overall CSI amplitude changes significantly as the dynamic component of the CSI rotates due to Doppler motion. Overall, the dynamic range of the CSI amplitude is analyzed in the simulation results [see Fig. 3(a)–(c)] based on the system model in Section II-B. The range, e.g., the detection sensitivity, increases as the $|h_{k,s}|/|h_{k,d}|$ increases, and saturates when the ratio is equal to or greater than 1 [see Fig. 3(a) and (b)]. The overall CSI phase change becomes linear (without aliasing) to the Doppler motion when the ratio exceeds 1 [see Fig. 3(c) and (d)].[1] Hence, ideally, the detection is at its optimal when $|h_{k,s}|/|h_{k,d}|$ is adjusted to approximately 1. Albeit any value greater than 1 has a similar dynamic range for the overall CSI amplitude, the beam pattern becomes increasingly monotone when $|h_{k,s}|/|h_{k,d}| \gg 1$, which

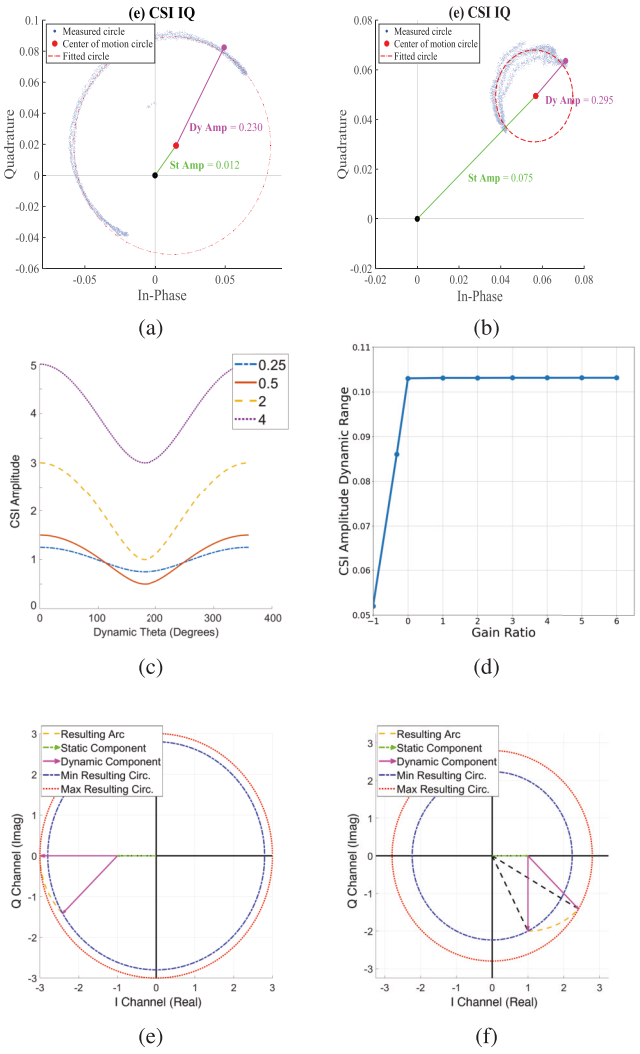

Fig. 3. CSI gain ratio effects. (a) CSI with small $|h_{k,s}|/|h_{k,d}|$ has a small dynamic range for its amplitude. (b) CSI with large $|h_{k,s}|/|h_{k,d}|$ has a large dynamic range for its amplitude. (c) Simulations show how the overall CSI amplitude changes at different $|h_{k,s}|/|h_{k,d}|$. (d) Simulation results show the dynamic range of the overall CSI amplitude changes at different $|h_{k,s}|/|h_{k,d}|$, where the x-axis denotes the ratio with a logarithmic scale. (e) Phase-aligned static and dynamic components reduce the overall CSI amplitude. (f) Phase-orthogonal static and dynamic components increase the overall CSI amplitude change.

[1] Under a realistic setting with the TX–RX synchronization error, the phase tuning effect is not pronounced as the phase noise overwhelms the phase changes introduced by the physiological motion.

reduces the mmWave communication reliability as the single LoS beam is vulnerable to blockage.

2) Global Phase Offset Tuning: Single-beam systems also suffer from the issue of null detection points as illustrated in Fig. 3(e) and (f). When the static and dynamic components are aligned with each other, e.g., $\angle h_{k,s}/h_{k,d} = 0^\circ$ or 180°, the change in amplitude of the CSI is small and nonlinear, contrary to when the static and dynamic components are orthogonal with each other, e.g., $\angle h_{k,s}/h_{k,d} = \pm 90^\circ$, and the change in the amplitude of the CSI is clear and linear. This phenomenon, where sensitivity is minimized when the static and dynamic paths interfere maximally (constructively or destructively), is consistent with the predictions of the Fresnel zone model [10]. Specifically, these null detection points often correspond to locations where the dynamic path reflector (e.g., the chest during breathing) lies near the boundary of a Fresnel zone, resulting in minimal signal amplitude change for small phase shifts.

For a single-beam system, $\angle h_{k,s}/h_{k,d}$ cannot be changed as it is only related to the length differences for the LoS and non-LoS (NLoS) paths. However, for a multibeam system, the global initial phase for each subarray can be individually tuned. Hence, the system can control the phase difference and "rotate" the dynamic component out of the null position for better detection.

Note that, although wideband signals such as OFDM provide multiple subcarriers at different frequencies, the spacing between subcarriers is fixed, meaning the phase offset achieved via channel selection is also fixed. There is a possibility that none of the subcarriers give good CSI amplitude readings due to an undesired $\angle h_{k,s}/h_{k,d}$ for sensing. The continuous global phase offset tuning provides fine-grained tuning to address this issue. Furthermore, even if the $h_{k,d}$ arc is larger than 180° and nonlinear mapping from $\angle h_{k,d}$ to $|h_k|$ is unavoidable, adjusting phase offset will provide linearity at different segments of $\angle h_{k,d}$, when it is mapped to $|h_k|$, which can be used for the recovery of the shape of the waveform.

C. Making Multibeam Practical: APA

APA architecture is a low-cost implementation of a multibeam system, meant to address the reliability challenges inherent in mmWave networks. Some mmWave transceivers use a full-MIMO architecture, with each RF chain linked to a single passive antenna, enabling flexible array processing and multibeam pattern synthesis. However, the hardware complexity limits scalability, as adding antennas demands more RF chains, significantly increasing cost, size, and power consumption [41]. Whereas, APA provides a contrasting cost-effective approach to connect multiple phased arrays to a single RF chain through a single combiner. Furthermore, a single array faces two critical challenges: limited field of view (FoV) and high directionality, which restricts its coverage. Typically, a phased array has a FoV narrower than $\pm 60^\circ$, limiting its ability to provide comprehensive coverage.

An APA architecture can be a viable approach in overcoming such FoV limitation, where multiple phased arrays are co-located to jointly cover 360° in azimuth or elevation while sharing the same RF chain but pointing at different angles. This aggregation allows for more effective utilization of the directional gain inherent in phased arrays, which is proportional to the number of antenna elements [39]. In this design, APAs were employed where one phased array was used for LoS communication while the other was used for both communication and sensing through beam steering.

IV. Experiments and Evaluations

The experimental datasets were obtained and validated using a SideSense prototype, a custom duo-TX, and a single-RX mmWave OFDM JCS system. The data include CSI recordings of sinusoidal motion executed by a mechanical mover and respiratory motion from three human subjects.

The SideSense prototype uses a 28-GHz OFDM waveform. The system uses baseband Universal Software Radio Peripheral (USRP) devices to modulate and demodulate OFDM signals. The transmitting USRP generates a 3.5-GHz signal at -15 dBm, which is up-converted to a 28-GHz waveform using an up/down converter. The output signal is power divided and drives two TMYTEK BBox Lite phased array TXs. Another USRP collects the signal from a single-phased array TMYTEK BBox RX. The OFDM waveform comprises 52 subcarriers over a 1-MHz bandwidth sampled at 625 Hz. The TX and RX subbeams have a 3-dB beamwidth of 25°.

One of the TX phased arrays, TX_s, is used as a communication subbeam. The other TX phased array, TX_d, is the sensing subbeam, which targets and narrows down the location of the moving subject. The resultant combination of the communication and sensing parts is recorded by the RX in both default and beamformed settings.

Fig. 4 shows the experimental arrangement of the communication setting, Joint communication and sensing setting, and sensing setting. Fig. 5 shows the experimental setup configuration of the mechanical mover in relation to the two TX and RX antennas from both a bird's-eye view and a side view. The TX and RX antennas are placed 1.08 m apart. The robotic mover consists of a single-axis stepper drive mount (Griffin Motion LNS-100 series linear stage) controlled by the Galil DMC30010 motion controller, set at a 115200 baud rate. The reflective surface of the mover is a flat rectangular metal plate measuring 20 cm by 15 cm. The face of the metal plate is aligned with the elevation level of the TX and RX antennas. The robotic mover is actuated using a Python script that implements the "gclib" library developed by the manufacturers.

A. Phantom Test With Linear Stage

For the initial experiment, the experimental setup is tested for an increase in sensing detection accuracy by beamforming the sensing TX_d. Both the TX and the RX phased array antennas have a beam steering capability between 45° and -45° with a resolution of 5° from the center. The TX antennas have beam steering in the azimuth angle, and the RX antenna can steer both in azimuth and elevation angles. The mover is placed at 30° angle from both Tx and Rx antennas. The mover is set to a frequency of 0.3 Hz at 1 cm peak-to-peak amplitude. The dataset is acquired by steering the sidelobe TX antenna (TX_d) from 0° to 45° with increments of 5°.

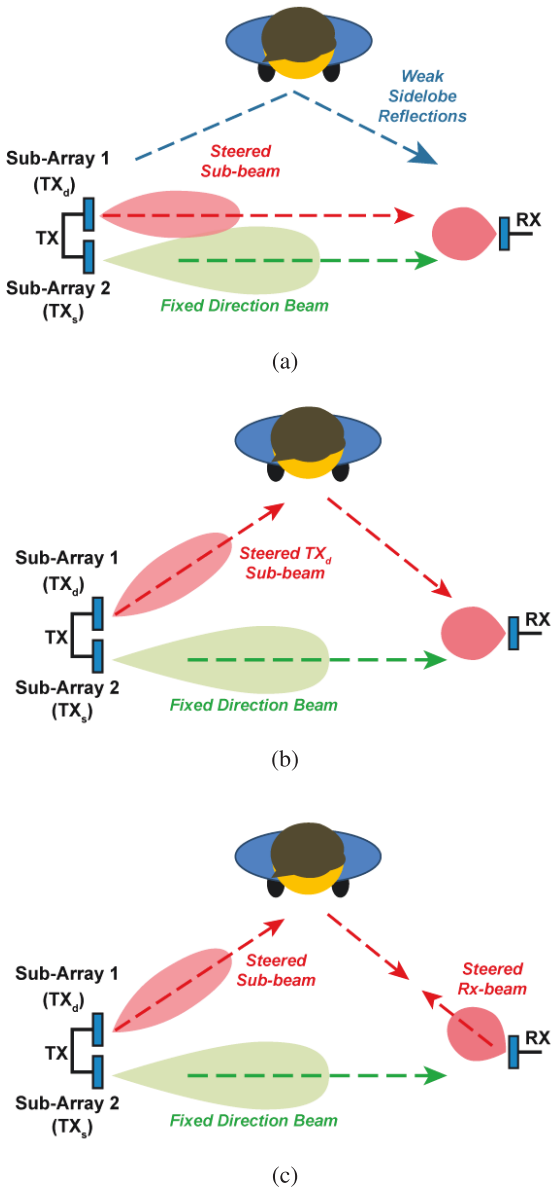

Fig. 4. IQ graph of sinusoidal motion for selected channels. (a) TX_d and TX_s point toward RX. (b) TX_d points toward the target and TX_s points toward RX. (c) TX_d and RX point toward the target. Multiple channel selection in OFDM systems is advantageous as the motion arcs are created at different dynamic angles, increasing the likelihood of an optimum position even for small movement sensing.

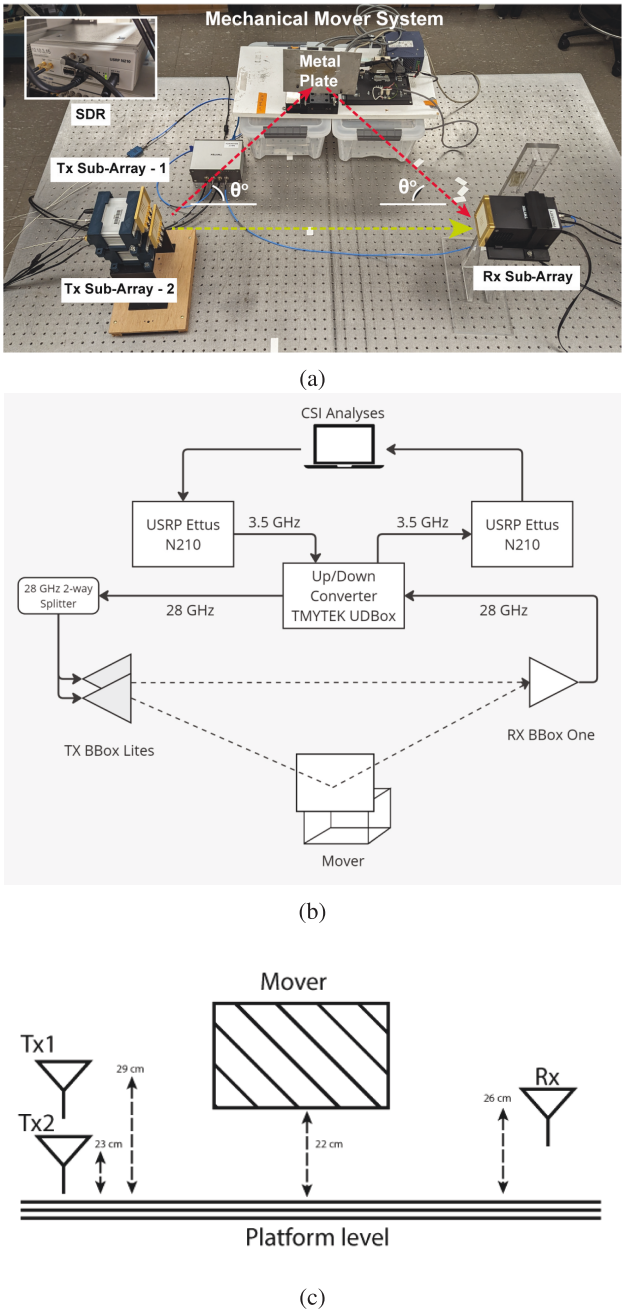

Fig. 5. (a) Experimental setup with mechanical mover and SideSense system. Schematic of experimental setup with (b) system block diagram and (c) height measurements.

Table II demonstrates the inverse relation between the SSNR of the amplitude and phase as the sensing subbeam is steered toward the target. For this experiment, there is a significant change in SSNR in both amplitude and phase measurements as the beam steers toward the target. The table provides an average change, whereas individual channels have optimum sensing settings at different beam angles. The average relation between the static and dynamic components has the highest orthogonality at 15°, maximizing the average magnitude SSNR. Conversely, the average phase SSNR increases as the alignment of static and dynamic components increases with TX_d angle.

Phase tuning is beyond the scope of this work, because: 1) the commercial off-the-shelf beamformer used in this work does not support a customized beamforming vector, and thus the phase tuning strategy cannot directly be implemented in the experiment, and 2) the static and dynamic components of the channel are determined by the physical environment, which can be complex in an indoor multipath setting, so strategically implementing gain tuning is also challenging in a naturally uncontrollable environment. However, the results from this initial experiment implicitly indicate the effects of gain and phase tuning, which align with our simulation observations. Furthermore, the results in this table demonstrate the effect of the sidelobe angle impacting SSNR. In addition, a greater number of available channels and wider system bandwidth expand phase and amplitude variation,

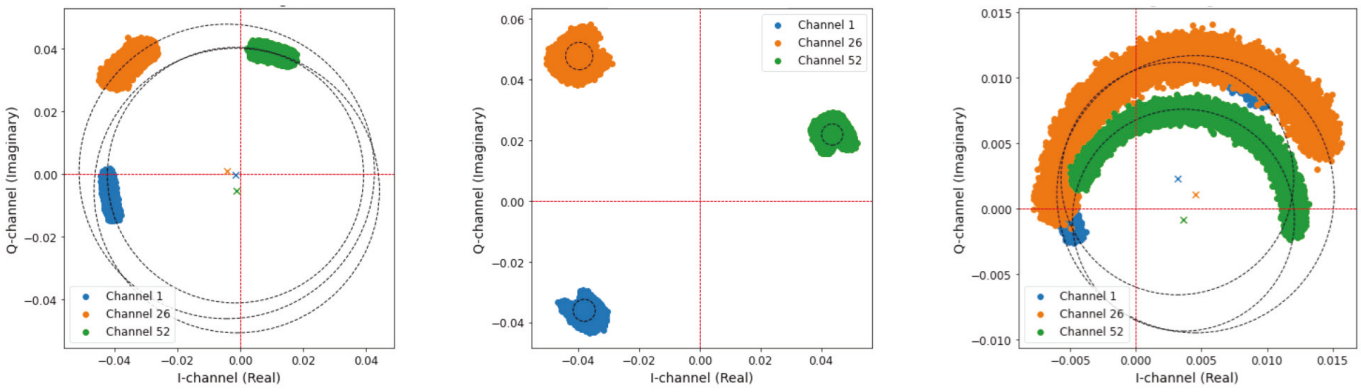

Fig. 6. IQ graph of sinusoidal motion for selected channels. (a) TX_d and TX_s point toward RX. (b) TX_d points toward the target and TX_s points toward RX. (c) TX_d and RX point toward the target. Multiple channel selection in OFDM systems is advantageous as the motion arcs are created at different dynamic angles, increasing the likelihood of an optimum position even for small movement sensing.

TABLE I

SYMBOLS USED IN EQUATIONS WITH THEIR MEANINGS IN MMWAVE COMMUNICATION AND SENSING

Symbol	Meaning	Dimension / Type
h_k	CSI at OFDM sub-carrier k	Complex Scalar
$h_{k,s}$	Static component of CSI	Complex Scalar
$h_{k,d}(t)$	Dynamic component of CSI	Complex Scalar
$\Delta\varphi(t)$	Phase difference between components	Scalar
d_s	Length of static signal path	Scalar
$d_d(t)$	Length of dynamic signal path	Scalar
λ_k	Wavelength at sub-carrier k	Scalar
y	Received signal at RX	Complex Scalar
$\mathbf{w_s}$	Static component beamforming weights	1 x N Complex Vector
$\mathbf{w_d}$	Dynamic component beamforming weights	1 x N Complex Vector
$\mathbf{h_s}$	Static component channel vector	1 x N Complex Vector
$\mathbf{h_d}$	Dynamic component channel vector	1 x N Complex Vector
x	Transmitted signal	Complex Scalar
z	Channel noise	Complex Scalar
N	Number of antenna elements in ULA	Scalar
a_s	Static component channel gain	Complex Scalar
a_d	Dynamic component channel gain	Complex Scalar
ϕ_s	Static component AoD	Scalar
ϕ_d	Dynamic component AoD	Scalar
d	Space between antenna elements	Scalar
$g_{s,n}$	Gain for n-th antenna (static)	Scalar
$g_{d,n}$	Gain for n-th antenna (dynamic)	Scalar
$\theta_{s,n}$	Phase for n-th antenna (static)	Scalar
$\theta_{d,n}$	Phase for n-th antenna (dynamic)	Scalar
Δ_s	Static component global phase offset	Scalar
Δ_d	Dynamic component global phase offset	Scalar
f_{phy}	Physiological motion frequency	Scalar
$\psi_b(t)$	Beam sweep evaluation metric	Scalar
Ψ_b	Beam sweep termination threshold	Scalar
$\psi_g(t)$	Gain ratio tuning metric	Scalar
Ψ_g	Gain tuning termination threshold	Scalar
δg	Gain tuning incrementing step	Scalar
$\psi_p(t)$	Phase offset tuning metric	Scalar
Ψ_p	Phase tuning termination threshold	Scalar
$\delta\phi$	Phase tuning incrementing step	Scalar

TABLE II

AVERAGE AMPLITUDE AND PHASE SSNR FOR DIFFERENT TX_D ANGLES

TX_d Angle (°)	Average Mag. SSNR	Average Phase SSNR
15	571.09	53.20
20	281.70	22.02
25	205.20	182.69
30	39.15	520.77

increasing the likelihood of an optimal channel for both functions.

The second set of experiments involves sinusoidal motion performed by the mover at eight different nominal distances, 0.45 cm apart. The mover is placed at a 45° angle with the TX antennas and the RX. The sinusoidal motion set at a frequency of 0.3 Hz and an amplitude of 0.45 cm peak-to-peak was chosen as a placeholder for respiratory motion simulation. The data were collected with the RX and TX_d beamformed at every combination of 0° and 45° angles of the sidelobe TX and the RX. The data are captured, and post-processing is done using Python scripts.

Fig. 6 shows the IQ graph of CSI of the recorded data with the real part assigned as the *I*-channel and the imaginary part assigned as the *Q*-channel. When all TX and RX antennas are in a direct LoS setting, it is denoted as the communication setting. When the sensing TX_d is beamformed toward the target, the setting is denoted as the JCS setting. When the sensing TX_d and the RX are both beamformed toward the moving target, the setting is called a sensing setting where the CCC is reduced the most.

The IQ graph shows the reduction of overall channel amplitude due to the minimum contribution of the communication channel in the sensing setting. For the work, the focus, measurement, and comparisons in sensing capabilities were carried out by taking the absolute value of CSI or the amplitude. OFDM systems are susceptible to phase noise; therefore, amplitude was considered as the more reliable measure of performance.

Multiple channels are analyzed for channel capacity measurement and respiration frequency detection. The difference in frequency modulations between consecutive channels provides higher frequency diversity to the experiments. The relative average positions with respect to the center of the dynamic offset depend on the frequency of the channels. Therefore, a number of IQ arcs are more likely to be in the optimum position for movement sensing.

Figs. 7 and 8 show the amplitude in the time and frequency domains, respectively. The amplitude measurement shows a higher static component, and therefore, channel capacity in the communication and JCS setting due to the contribution of the

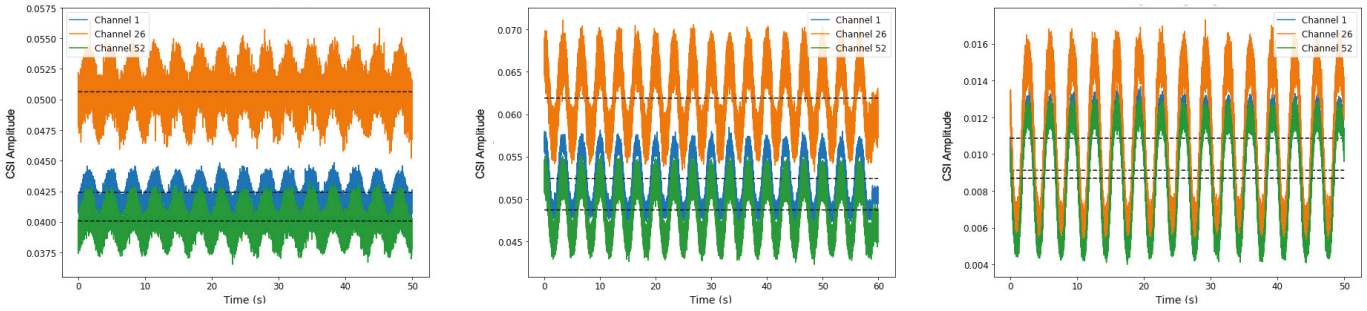

(a) (b) (c)

Fig. 7. Time domain CSI amplitude of sinusoidal motion for selected channels. (a) TX_d and TX_s point toward RX. (b) TX_d points toward the target and TX_s points toward RX. (c) TX_d and RX point toward the target. The black dotted line denotes average CSI amplitude. Differences in CSI amplitude for subcarriers 1, 26, and 52 are due to frequency diversity and Rayleigh fading.

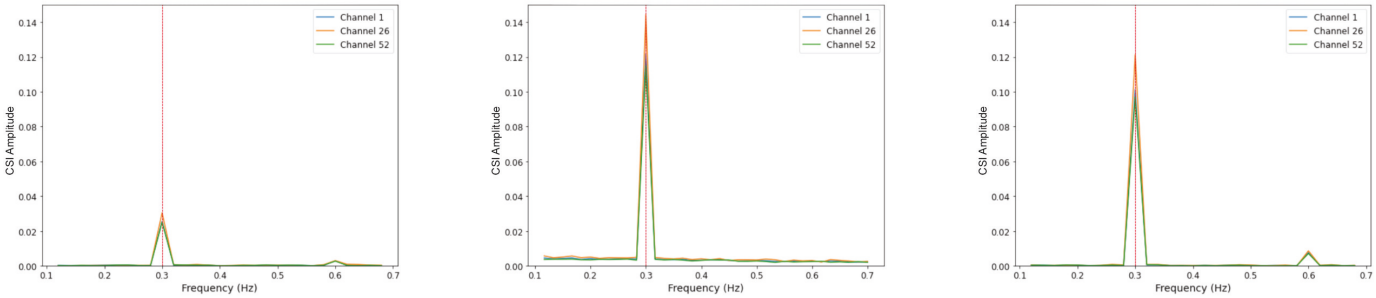

(a) (b) (c)

Fig. 8. Frequency domain CSI amplitude of sinusoidal motion for selected channels. (a) TX_d and TX_s point toward RX. (b) TX_d points toward the target and TX_s points toward RX. (c) TX_d and RX point toward the target.

communication TX_s. It is also to be noted that the difference between the detection of the target frequency is comparable in both JCS and sensing settings. In the JCS setting, the static versus dynamic offset is higher than in the sensing setting. This change is reflected in the slightly improved detection of the target frequency in the JCS setting.

B. Human Data Collection

The sinusoidal motion does not accurately represent an actual breathing waveform. True respiration has variances in the durations of inhalation and exhalation. Moreover, the shapes of periodic motion vary from the true sinusoidal signal and differ for each person. Therefore, respiratory data from three consenting human subjects were collected with photoplethysmography (PPG) as a reference.

For data collection, the subjects were seated with their torso facing toward the setup and angled at 30° from the RX and TX antennas. The respiratory rate of 15 bpm was chosen to be close to the human resting breathing rate. For each subject, three data instances were collected over a duration of 2 min. The data were recorded with the Tx_d–Rx settings beamsteered at 0°–0°, 30°–0°, and 30°–30°.

Fig. 9 shows the difference in IQ plots taken in the communication and sensing settings. Considering that the human thorax moves close to 1 cm during respiration, the total phase change should be higher in an ideal case. However, the nonuniform shape of the human thorax means that the displacement varies in different parts of the thorax. Depending on the position of the thorax a narrow beam focuses on, it is possible to get readings of a smaller displacement in the CSI recordings.

Fig. 10 demonstrates the improvement of respiratory signal detection as the radar system is configured toward the communication setting and the sensing setting. The improvement in the ratio of the static and dynamic components contributes to this. The uneven nature of the human thorax creates increased scattering and multipath, therefore, resulting in increased noise. The FFT was performed over 40 s of data captured at a sampling rate of 625 Hz for each channel.

C. Results

The performance comparison of the three settings is calculated using the CCC and the SSNR. The CCC is evaluated based on the Shannon capacity computed via the following equation:

$$\mathrm{CCC} = \sum_{k=1}^{52} \mathrm{BW} \log_2 \left(1 + \frac{P_t}{N_0} E\left(|h_k|\right)\right) \tag{13}$$

where BW is the subcarrier bandwidth, $P_t = -10$ dBm is the transmitting power, $N_0 = -70$ dBm is the noise floor variance, and $E(\cdot)$ is the expected value.

The sensing performance is evaluated based on the SSNR of the physiological motion versus the environment noise

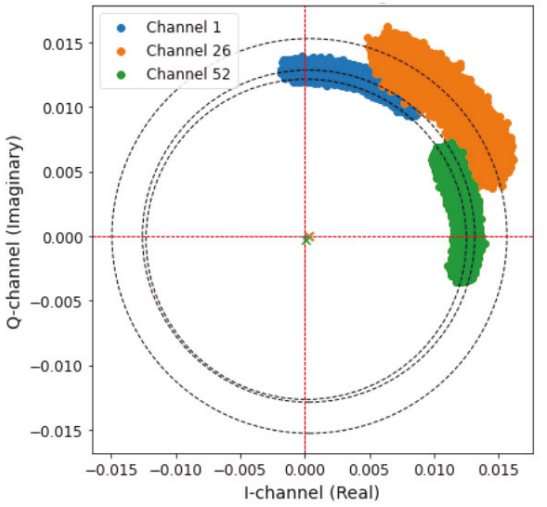

(a)

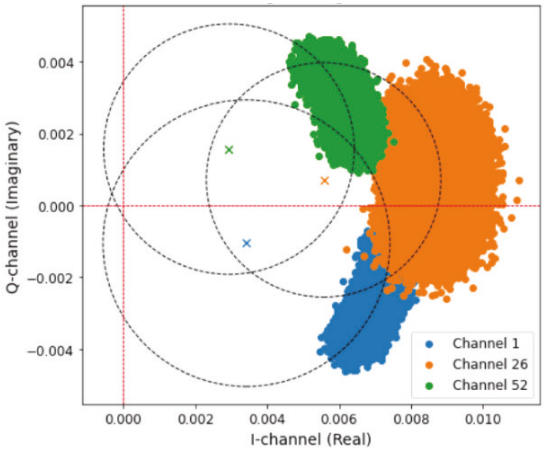

(b)

Fig. 9. IQ plots of CSI data of human subject respiration for two scenarios. (a) TX_d and TX_s point toward RX. (b) TX_d and RX point toward the target.

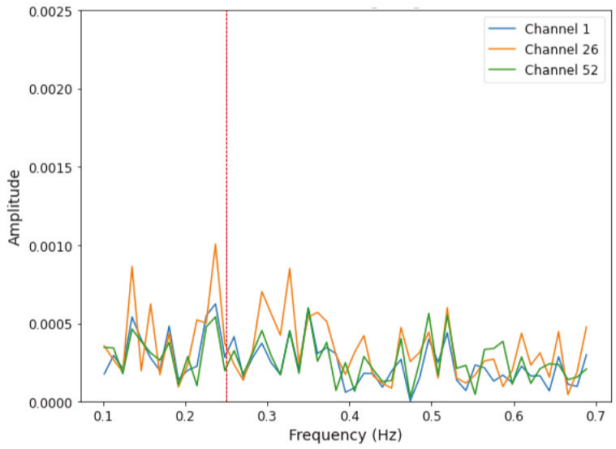

(a)

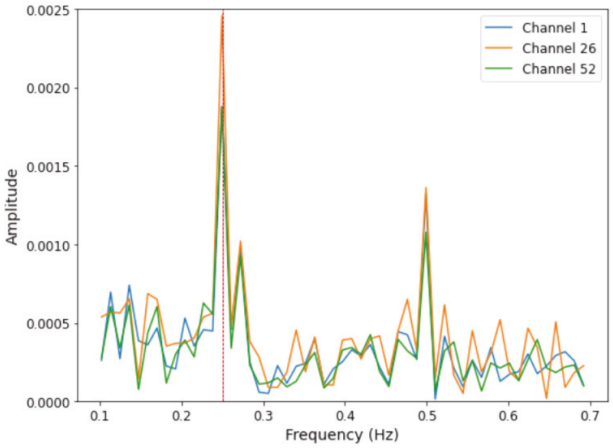

(b)

Fig. 10. FFT plots of CSI amplitude recorded with a human subject for two scenarios. (a) TX_d and TX_s point toward RX. (b) TX_d and RX point toward the target.

TABLE III
CCC AND SSNR CHART OF MOTION EXPERIMENTS WITH THE RADAR SYSTEM AT COMMUNICATION, JCS, AND SENSING SETTINGS

		Mover (0.3 Hz)	Subject 1	Subject 2	Subject 3
CCC (Mbps)	Communication	11.16	7.75	8.05	10.98
	JCS	11.74	11.16	11.44	10.03
	Sensing	6.72	6.09	6.04	5.01
SSNR	Communication	116	3.15	7.78	4.79
	JCS	193	4.05	3.05	8.06
	Sensing	710	7.58	8.16	10

evaluated at the frequency domain after the fast Fourier transform, e.g., Algorithm 1, recited below

$$\text{SSNR} = \frac{H\left(f = f_{\text{phy}}\right)}{E\left(H\left(f \neq f_{\text{phy}}\right)\right)}. \tag{14}$$

Table III illustrates the change in CCC and SSNR in the three settings of the radar system. A clear improvement in SSNR is shown in the radar settings as the system is configured from a purely communication to a purely sensing mode. The CCC decreases more for the JCS setting than in the purely communication setting. This can be explained by the use of two TX antennas acting as the communication antenna and the sensing antenna. Due to phase misalignment at the RX point, the communication setting suffers. This is constant throughout all the experiments, as the setup was kept identical between tests. The NLoS phase alignment is better during the JCS setting, slightly increasing the CCC.

Although a significant improvement of 84% is noticed for sensing modes in SSNR on average, the CCC decreases by 35% on average. The CCC of the purely communication mode can be further improved using phase tuning methods.

The variability in SSNR improvement among subjects is large due to differences in torso properties and scattering, which are more complex than the uniform reflections from a mechanical mover. For Subject 3, the smaller SSNR variation between the JCS and sensing settings likely results from subtler changes in the static-to-dynamic ratio of the CSI, driven by the subject's unique torso geometry and positioning relative to the beams.

V. CONCLUSION

A low-cost mmWave JCS system based on an APA architecture named SideSense was presented for physiological motion

sensing. The system is compatible with FutureG wireless communication system architectures currently being standardized by 3GPP and 802.11 workgroups. Findings through Fresnel zone analysis of the JCS channel mode show that maintaining power ratio between the communication subbeam and sensing subbeam greater than 1 is preferred to jointly optimize the SSNR and CCC, whereas a global phase difference of a $\pm 90^\circ$ between communication and sensing subbeams is favored to maximize the physiological motion's presence in the composite CSI. A prototype of SideSense has been developed with 28-GHz beamformers and SDRs, and phantom and human subjects' tests were presented to highlight its performance. The current SideSense design is optimized for focused TX–RX setups, and promising results have been observed in stationary, single-subject scenarios. The adaptation challenge for dynamic, multiperson, or motion scenarios is an opportunity for future research. Future work will also be needed to integrate phase shifters and amplifiers at each subarray to enable separated phase and gain tuning, achieving optimal phase and amplitude ratios for physiological motion detection.

REFERENCES

[1] L. G. de Oliveira, B. Nuss, M. B. Alabd, A. Diewald, M. Pauli, and T. Zwick, "Joint radar-communication systems: Modulation schemes and system design," *IEEE Trans. Microw. Theory Techn.*, vol. 70, no. 3, pp. 1521–1551, Mar. 2022. [Online]. Available: https://ieeexplore.ieee.org/document/9627227/

[2] J. Pegoraro, J. O. Lacruz, F. Meneghello, E. Bashirov, M. Rossi, and J. Widmer, "RAPID: Retrofitting IEEE 802.11ay access points for indoor human detection and sensing," *IEEE Trans. Mobile Comput.*, vol. 23, no. 5, pp. 4501–4519, May 2023. [Online]. Available: https://ieeexplore.ieee.org/document/10172159

[3] A. Schlegel and J. A. Nanzer, "Experimental demonstration of joint sensing and communications using spectrally efficient high-accuracy range estimation," *IEEE Trans. Microw. Theory Techn.*, vol. 72, no. 8, pp. 4900–4907, Aug. 2024. [Online]. Available: https://ieeexplore.ieee.org/document/10453407/

[4] M. Temiz, C. Horne, N. J. Peters, M. A. Ritchie, and C. Masouros, "An experimental study of radar-centric transmission for integrated sensing and communications," *IEEE Trans. Microw. Theory Techn.*, vol. 71, no. 7, pp. 3203–3216, Jul. 2023. [Online]. Available: https://ieeexplore.ieee.org/document/10018010/

[5] J. A. Zhang et al., "Enabling joint communication and radar sensing in mobile networks—A survey," *IEEE Commun. Surveys Tuts.*, vol. 24, no. 1, pp. 306–345, 1st Quart., 2022. [Online]. Available: https://ieeexplore.ieee.org/document/9585321

[6] Q. Zhang, X. Wang, Z. Li, and Z. Wei, "Design and performance evaluation of joint sensing and communication integrated system for 5G mmWave enabled CAVs," *IEEE J. Sel. Topics Signal Process.*, vol. 15, no. 6, pp. 1500–1514, Nov. 2021. [Online]. Available: https://ieeexplore.ieee.org/document/9528013

[7] F. Zhao et al., "A Ka-band 4TX/4RX dual-stream joint radar-communication phased-array CMOS transceiver," *IEEE Trans. Microw. Theory Techn.*, vol. 72, no. 3, pp. 1993–2008, Mar. 2024. [Online]. Available: https://ieeexplore.ieee.org/document/10264109/

[8] J. Deng, P. Burasa, and K. Wu, "Joint multiband linear interferometric receiver for integrated microwave and terahertz sensing and communication systems," *IEEE Trans. Microw. Theory Techn.*, vol. 72, no. 9, pp. 5550–5562, Sep. 2024. [Online]. Available: https://ieeexplore.ieee.org/document/10433911/

[9] Z. Fang et al., "A silicon-based radio platform for integrated edge sensing and communication toward sustainable healthcare," *IEEE Trans. Microw. Theory Techn.*, vol. 71, no. 3, pp. 1296–1311, Mar. 2023. [Online]. Available: https://ieeexplore.ieee.org/document/9959877/

[10] D. Zhang, H. Wang, and D. Wu, "Toward centimeter-scale human activity sensing with Wi-Fi signals," *Computer*, vol. 50, no. 1, pp. 48–57, Jan. 2017. [Online]. Available: https://ieeexplore.ieee.org/document/7807197

[11] Y.-S. Huang, X. Yang, L. Zhou, C. Gu, and J. Mao, "Long-range vital sign monitoring by using a W band heterogeneously integrated FMCW radar sensor," in *IEEE MTT-S Int. Microw. Symp. Dig.*, Denver, CO, USA, Jun. 2022, pp. 1044–1047. [Online]. Available: https://ieeexplore.ieee.org/document/9865279/

[12] S. M. M. Islam, N. Motoyama, S. Pacheco, and V. M. Lubecke, "Non-contact vital signs monitoring for multiple subjects using a millimeter wave FMCW automotive radar," in *IEEE MTT-S Int. Microw. Symp. Dig.*, Los Angeles, CA, USA, Aug. 2020, pp. 783–786. [Online]. Available: https://ieeexplore.ieee.org/document/9223838/

[13] W. Kang, C. Zhou, and W. Wu, "Respiration monitoring of all occupants in a vehicle using time-division multiplexing FMCW radar based on metasurface technology," *IEEE Trans. Microw. Theory Techn.*, vol. 72, no. 8, pp. 4960–4974, Aug. 2024. [Online]. Available: https://ieeexplore.ieee.org/document/10449949/

[14] E. Cardillo, L. Ferro, G. Sapienza, and C. Li, "Reliable eye-blinking detection with millimeter-wave radar glasses," *IEEE Trans. Microw. Theory Techn.*, vol. 72, no. 1, pp. 771–779, Jan. 2024. [Online]. Available: https://ieeexplore.ieee.org/document/10314454/

[15] J. Zhang, J. Qiu, K. Wang, K. Fang, A. K. Bashir, and W. Wang, "Millimeter-wave radar-based unsteady vital signs monitoring for smart home," in *Proc. IEEE Int. Conf. Commun. (ICC)*, Jun. 2024, pp. 3358–3364. [Online]. Available: https://ieeexplore.ieee.org/document/10622996

[16] A. Adhikari and S. Sur, "MiSleep: Human sleep posture identification from deep learning augmented millimeter-wave wireless systems," *ACM Trans. Internet Things*, vol. 5, no. 2, pp. 1–33, Mar. 2024. [Online]. Available: https://dl.acm.org/doi/10.1145/3643866

[17] H. Yin et al., "Let IoT know you better: User identification and emotion recognition through millimeter-wave sensing," *IEEE Internet Things J.*, vol. 10, no. 2, pp. 1149–1161, Jan. 2023. [Online]. Available: https://ieeexplore.ieee.org/document/9878260

[18] P. Mehrjouseresht, R. E. Hail, P. Karsmakers, and D. M. M.-P. Schreurs, "Respiration and heart rate monitoring in smart homes: An angular-free approach with an FMCW radar," *Sensors*, vol. 24, no. 8, p. 2448, Apr. 2024, doi: 10.3390/s24082448.

[19] J. Xiong, H. Hong, H. Zhang, N. Wang, H. Chu, and X. Zhu, "Multitarget respiration detection with adaptive digital beamforming technique based on SIMO radar," *IEEE Trans. Microw. Theory Techn.*, vol. 68, no. 11, pp. 4814–4824, Nov. 2020. [Online]. Available: https://ieeexplore.ieee.org/document/9198909

[20] M. Nosrati, S. Shahsavari, S. Lee, H. Wang, and N. Tavassolian, "A concurrent dual-beam phased-array Doppler radar using MIMO beamforming techniques for short-range vital-signs monitoring," *IEEE Trans. Antennas Propag.*, vol. 67, no. 4, pp. 2390–2404, Apr. 2019. [Online]. Available: https://ieeexplore.ieee.org/document/8621039/

[21] Z. Xu et al., "Simultaneous monitoring of multiple people's vital sign leveraging a single phased-MIMO radar," *IEEE J. Electromagn., RF Microw. Med. Biol.*, vol. 6, no. 3, pp. 311–320, Sep. 2022. [Online]. Available: https://ieeexplore.ieee.org/document/9716146/

[22] P.-H. Juan, C.-Y. Chueh, and F.-K. Wang, "Distributed MIMO CW radar for locating multiple people and detecting their vital signs," *IEEE Trans. Microw. Theory Techn.*, vol. 71, no. 3, pp. 1312–1325, Mar. 2023. [Online]. Available: https://ieeexplore.ieee.org/document/9938410

[23] X. Zhang, Y. Zeng, W. Wang, and B. S. Lim, "Joint radar and communication with 5G signal: Algorithms, prototypes and experiments," in *Proc. IEEE VTS Asia Pacific Wireless Commun. Symp. (APWCS)*, Aug. 2024, pp. 1–5. [Online]. Available: https://ieeexplore.ieee.org/document/10679307

[24] P. Kumari, N. Gonzalez-Prelcic, and R. W. Heath Jr., "Investigating the IEEE 802.11ad standard for millimeter wave automotive radar," in *Proc. IEEE 82nd Veh. Technol. Conf. (VTC-Fall)*, Sep. 2015, pp. 1–5. [Online]. Available: https://ieeexplore.ieee.org/document/7390996

[25] V. Va and R. W. Heath Jr., "Performance analysis of beam sweeping in millimeter wave assuming noise and imperfect antenna patterns," in *Proc. IEEE 84th Veh. Technol. Conf. (VTC-Fall)*, Sep. 2016, pp. 1–5. [Online]. Available: https://ieeexplore.ieee.org/document/7881150

[26] J. Pegoraro et al., "JUMP: Joint communication and sensing with unsynchronized transceivers made practical," *IEEE Trans. Wireless Commun.*, vol. 23, no. 8, pp. 9759–9775, Aug. 2024. [Online]. Available: https://ieeexplore.ieee.org/document/10443836

[27] Y. R. Li, B. Gao, X. Zhang, and K. Huang, "Beam management in millimeter-wave communications for 5G and beyond," *IEEE Access*, vol. 8, pp. 13282–13293, 2020. [Online]. Available: https://ieeexplore.ieee.org/document/8947954/

[28] Q. Xue et al., "A survey of beam management for mmWave and THz communications towards 6G," 2023, *arXiv:2308.02135*.

[29] K. M. Ishmael, Y. Pan, D. Landika, Y. Zheng, V. M. Lubecke, and O. Boric-Lubecke, "Physiological motion sensing via channel state information in NextG millimeter-wave communications systems," *IEEE J. Microw.*, vol. 3, no. 1, pp. 227–236, Jan. 2023. [Online]. Available: https://ieeexplore.ieee.org/document/9985013

[30] K. Ishmael, E. Lan, R. Ordonez, Y. Zheng, V. Lubecke, and O. Borić - Lubecke, "Heart signal sensing using millimeter-wave OFDM waveform in FutureG communications systems," in *Proc. 21st Eur. Radar Conf. (EuRAD)*, Sep. 2024, pp. 75–78.

[31] C. Qi, W. Ci, J. Zhang, and X. You, "Hybrid beamforming for millimeter wave MIMO integrated sensing and communications," 2022, *arXiv:2203.06324*.

[32] E. Perahia and M. X. Gong, "Gigabit wireless LANs: An overview of IEEE 802.11ac and 802.11ad," *ACM SIGMOBILE Mobile Comput. Commun. Rev.*, vol. 15, no. 3, pp. 23–33, Nov. 2011, doi: 10.1145/2073290.2073294.

[33] T. Nitsche, C. Cordeiro, A. Flores, E. Knightly, E. Perahia, and J. Widmer, "IEEE 802.11ad: Directional 60 GHz communication for multi-gigabit-per-second Wi-Fi [invited paper]," *IEEE Commun. Mag.*, vol. 52, no. 12, pp. 132–141, Dec. 2014. [Online]. Available: https://ieeexplore.ieee.org/document/6979964

[34] W. Hong, K.-H. Baek, Y. Lee, Y. Kim, and S.-T. Ko, "Study and prototyping of practically large-scale mmWave antenna systems for 5G cellular devices," *IEEE Commun. Mag.*, vol. 52, no. 9, pp. 63–69, Sep. 2014. [Online]. Available: https://ieeexplore.ieee.org/document/8316768

[35] Y. Huang, Y. Li, H. Ren, J. Lu, and W. Zhang, "Multi-panel MIMO in 5G," *IEEE Commun. Mag.*, vol. 56, no. 3, pp. 56–61, Mar. 2018. [Online]. Available: https://ieeexplore.ieee.org/document/8316768

[36] W. Kim, J. Bae, and S.-J. Lee, "Gain degradation effect due to beam misalignment on mmWave beamforming for 5G cellular communication," in *Proc. Int. Conf. Inf. Commun. Technol. Converg. (ICTC)*, Oct. 2015, pp. 1252–1256. [Online]. Available: https://ieeexplore.ieee.org/document/7354789s

[37] M. Giordani, M. Polese, A. Roy, D. Castor, and M. Zorzi, "A tutorial on beam management for 3GPP NR at mmWave frequencies," *IEEE Commun. Surveys Tuts.*, vol. 21, no. 1, pp. 173–196, 1st Quart., 2019. [Online]. Available: https://ieeexplore.ieee.org/document/8458146

[38] A. Ichkov, I. Gehring, P. Mähönen, and L. Simić, "Millimeter-wave beam misalignment effects of small{-} and large-scale user mobility based on urban measurements," in *Proc. 5th ACM Workshop Millim.-Wave Terahertz Netw. Sens. Syst.*, Oct. 2021, pp. 13–18, doi: 10.1145/3477081.3481672.

[39] S. Wang, J. Huang, X. Zhang, H. Kim, and S. Dey, "X-array: Approximating omnidirectional millimeter-wave coverage using an array of phased arrays," in *Proc. 26th Annu. Int. Conf. Mobile Comput. Netw.*, Apr. 2020, pp. 1–14, doi: 10.1145/3372224.3380882.

[40] I. K. Jain, R. Subbaraman, and D. Bharadia, "Two beams are better than one: Towards reliable and high throughput mmWave links," in *Proc. ACM SIGCOMM Conf.* New York, NY, USA: ACM, Aug. 2021, pp. 488–502, doi: 10.1145/3452296.3472924.

[41] K. Zheng, W. Zhao, T. Woodford, R. Zhao, X. Zhang, and Y. Hua, "Enhancing mmWave radar sensing using a phased-MIMO architecture," in *Proc. 22nd Annu. Int. Conf. Mobile Syst., Appl. Services*, Jun. 2024, pp. 56–69, doi: 10.1145/3643832.3661865.

Mohammad Shadman Ishrak (Graduate Student Member, IEEE) received the B.Sc. and M.Sc. degrees from the University of Dhaka, Dhaka, Bangladesh, in 2018 and 2020, respectively.

He is currently enrolled in the Ph.D. Program with the Department of ECE, University of Hawai'i at Manoā, Honolulu, HI, USA. His current work involves the analysis of demodulation techniques and their efficiency in Doppler radar signals for the application. His research interests include non-invasive vital sign detection, cardiorespiratory signal processing, and identity authentication and posture classification through RF sensors.

Jannatun Noor Sameera (Graduate Student Member, IEEE) received the B.S. and M.S. degrees in electrical and electronic engineering from the University of Dhaka, Dhaka, Bangladesh, in 2018 and 2020, respectively. She is currently pursuing the Ph.D. degree in electrical and computer engineering at the University of Hawai'i at Manoā, Honolulu, HI, USA.

Her current research interests include antenna design and applications, biomedical signal processing, physiological monitoring sensors, and wireless health monitoring systems.

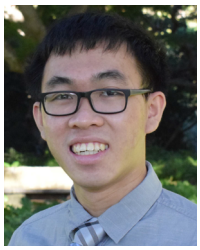

Alvin Yang (Graduate Student Member, IEEE) received the B.A. degree in computer engineering from the University of Hawai'i at Manoā, Honolulu, HI, USA, in 2020, where he is currently pursuing the M.S. degree at the Department of Electrical and Computer Engineering.

He is working as a Software Engineer with Nalu Scientific, Honolulu. His current research interests include the usage of millimeter waves and the novel uses of intelligent reflecting surfaces in wireless communications and sensing.

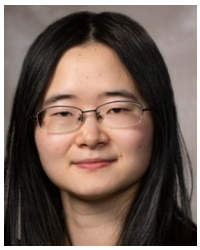

Yanjun Pan (Member, IEEE) received the bachelor's degree from Nanjing University of Aeronautics and Astronautics, Nanjing, China, in 2016, and the Ph.D. degree in electrical and computer engineering from the University of Arizona, Tucson, AZ, USA, in 2021.

She is an Assistant Professor with the Department of Electrical Engineering and Computer Science, University of Arkansas, Fayetteville, AR, USA. Her research interests include wireless security, information security, wireless sensing, and network optimization, emphasizing physical layer security, privacy-preserving technologies, millimeter-wave sensing, and cross-layer optimization.

Yao Zheng (Member, IEEE) received the B.S. degree in microelectronics from Fudan University, Shanghai, China, in 2007, the M.S. degree in electrical and computer engineering from Worcester Polytechnic Institute, Worcester, MA, USA, in 2011, and the Ph.D. degree in computer science from Virginia Polytechnic Institute and State University, Blacksburg, VA, USA, in 2019.

He is an Associate Professor with the Department of Electrical Engineering, University of Hawai'i at Mānoa, Honolulu, HI, USA. From 2024 to 2025, he was a Visiting Scientist with the Department of Electrical Engineering and Computer Science, Terahertz Integrated Electronics Group, Massachusetts Institute of Technology, Cambridge, MA, USA. His research interests include wireless communication, sensing, and security.

Olga Borić-Lubecke (Fellow, IEEE) received the B.Sc. degree in electrical engineering from the University of Belgrade, Belgrade, Serbia, in 1989, the M.S. degree in electrical engineering from the California Institute of Technology, Pasadena, CA, USA, in 1990, and the Ph.D. degree in electrical engineering from the University of California at Los Angeles, Los Angeles, CA, USA, in 1995.

She was with Bell Laboratories, Lucent Technologies, Murray Hill, NJ, USA; the Institute of Physical and Chemical Research (RIKEN), Sendai, Japan; and the NASA Jet Propulsion Laboratory, Pasadena, CA, USA, where she conducted research in RFIC technology and biomedical applications of wireless systems. She co-founded and was the Chief Technical Advisor of a start-up company, Kai Medical, Honolulu, HI, USA. She is a Professor of electrical and computer engineering with the University of Hawai'i at Manoā (UH), Honolulu. She is also a Co-Founder and the President of Adnoviv, Inc., Honolulu. She has authored more than 250 journal and conference publications, two books, and several book chapters. She holds three patents, and her research has been featured by various media outlets. Her research interests include wireless circuits and systems, biomedical applications, and renewable energy.

Prof. Borić-Lubecke is a Fulbright Senior Scholar, a Foreign Member of the Academy of Engineering of Serbia, and a Distinguished Member of the National Academy of Inventors, UH Chapter. She was a co-recipient of the Emerging Technology Award at TechConnect 2007. She was the adviser-author of several award-winning IEEE Microwave Theory and Techniques Society and IEEE Engineering in Medicine and Biology Society Student Papers. She was the Workshop Chair for the 2003 IEEE IMS, the Technical Program Vice-Chair for the 2007 IEEE IMS, the Technical Program Co-Chair for the 2017 IEEE IMS, and the 2018 IEEE IMS Technical Program Advisor. She was an Associate Editor of IEEE MICROWAVE AND WIRELESS COMPONENTS LETTERS and IEEE TRANSACTIONS ON MICROWAVE THEORY AND TECHNIQUES.

Victor M. Lubecke (Fellow, IEEE) received the B.S. degree in electrical and electronics engineering from California State Polytechnic University, Pomona, CA, USA, in 1986, and the M.S. and Ph.D. degrees in electrical engineering from the California Institute of Technology, Pasadena, CA, USA, in 1990 and 1995, respectively.

He was with the NASA Jet Propulsion Laboratory (JPL), Pasadena, CA, USA, and the Institute for Physical and Chemical Research (RIKEN), Wako, Japan, where his research involved terahertz and MEMS receiver technologies for space remote sensing and communications applications. He was previously with Bell Laboratories, Lucent Technologies, Murray Hill, NJ, USA, where his research focused on remote sensing technologies for biomedical and industrial applications and on microelectromechanical systems (MEMS) and 3-D wafer-scale integration technologies for wireless and optical communications. He also co-founded and served as a CTO for Kai Medical, Inc., Honolulu, and co-founded Adnoviv, Inc., Honolulu, where he serves as a Vice President. He is currently a Professor of electrical and computer engineering with the University of Hawai'i at Manoā, Honolulu. He has published more than 250 peer-reviewed research articles and holds eight U.S. patents. His current research interests include remote sensing, biomedical sensors, MEMS, heterogeneous integration, and microwave/terahertz radio.

Dr. Lubecke is a Fulbright Senior Scholar, an emeritus Distinguished Microwave Lecturer of the IEEE Microwave Theory and Techniques (MTT) Society, and a Speakers Bureau Speaker. He has served as a Topic Editor for IEEE TRANSACTIONS ON TERAHERTZ SCIENCE AND TECHNOLOGY, the Vice-Chair for the 2017 IEEE International Microwave Symposium (IMS), and a member of the MTT Technical Committees for Terahertz Technology and Applications and Biological Effects and Medical Applications.